Robust and accurate formulation for modeling of acid stimulation

Tomin, P.; Voskov, D.

DOI
10.3997/2214-4609.201802120

Publication date
2018

Document Version
Final published version

Published in
16th European Conference on the Mathematics of Oil Recovery, ECMOR 2018

Mo A1 12

Robust And Accurate Formulation For Modeling Of Acid Stimulation

P. Tomin (Stanford University), D. Voskov* (TU Delft)

Summary

Accurate representation of processes associated with energy extraction from subsurface formations often requires models which account for chemical interactions between different species in the presence of multiphase flow. In this study, we focus on modeling of acid stimulation in the near-well region. For the chemical processes which include a dissolution of rock material, an issue arises with the predictive representation of flow. Taking into account the spatial scale of discretization, some of simulation control volumes can have values of porosity close to 1, which makes an application of Darcy's law inconsistent and requires employing a true momentum equation such as the Darcy-Brinkman-Stokes (DBS) equation. The DBS equation automatically switches the description between Darcy equation in control volumes with low porosity and Stokes equation in grid blocks with high porosity. For chemical reactions, we propose a local nonlinear solution technique that allows solving the balance of solid species separately yet retaining the full coupling with rest of the equations. Finally, we study the impact of multiphase flow. The DBS approach is not well established for multiphase flow description. Therefore we employ a hybrid approach, where we assume that the single-phase DBS flow and the multiphase Darcy flow occur in separate regions. We test the accuracy and performance of both approaches on realistic models of practical interest.

Introduction

The near-well region is the most well known area of subsurface reservoir. The detailed description of near-well area helps to model various processes there and predict well productivity. These studies provide a better insight for well performance optimization and more accurate reservoir scale well approximation. The local changes in near-well characteristic caused by formation damage or stimulation (using either hydraulic fracturing or acidizing) have strong effect on well performance (Kalfayan, 2008). When the acid is injected above fracturing pressure in acidizing process, it is called fracture acidizing. The acid propagates across the fracture at elevated pressure which force farther development of fracture and subsequently deeper acid penetration into the reservoir. Alternative strategy is to inject the acid below the fracturing pressure where the acid forms wormholes and helps to overcome near-well damage. This strategy is the focus of our study.

Acidizing is one of the most employed stimulation techniques used in petroleum engineering. In 1994, 79% of the stimulation jobs in the petroleum industry were comprised only of acid stimulation (Earlougher Jr, 1977). Later, hydralic fracturing embraced a big portion of well stimulation activity. Still, the acidizing keeps an important portion of the stimulation jobs in the petroleum and geothermal fields. Accurate modeling of acidizing can help in a better prediction of risks and suggests an optimal operational regimes.

The governing models includes multiphase multicomponent reactive flow and transport. These models are quite sensitive to the spacial and temporal scales of representation (Golfier et al., 2002). For example, in practical simulation of acidizing process, the rock material in some of control volumes can be fully dissolved, which makes the assumption of Darcy's flow inaccurate and requires free flow or Stokes' assumptions. This problem can be resolved withing the application of the unified Darcy-Brinkman-Stokes (DBS) equation (Brinkman, 1949).

In this approach, the velocity description is switching between Darcy's assumptions in subsurface regions with natural porosity and Stokes assumptions in regions with high porosity. The large heterogeneities of porosity are directly accounted in the DBS formalism. Recently, the sequentially coupled reactive flow and transport based on DBS framework was proposed for pore-scale modeling (Soulaine and Tchelepi, 2016; Soulaine et al., 2017). Later, the DBS model was employed and tested for flow at the continuous scale (Shaik, 2017; Shaik et al., 2018).

In this work, we provide a detailed description of numerical framework based on DBS and present a comparison between Darcy and DBS models based on numerical implementation in the new version of Automatic Differentiation General Purpose Research Simulator (AD-GPRS) (AD-GPRS, 2018; Voskov et al., 2017; Rin et al., 2017; Rin, 2017; Garipov et al., 2018). In the first section, we will briefly describe governing equations for the proposed framework. In the second section, chemical model including constitutive relations for porosity, permeability and major dimensionless numbers used in analysis will be described. Third section will describe numerical methods used in the framework.

Finally, in fourth section, numerical results are present. Since the process is unstable, a point-by-point analysis of dissolution patterns is meaningless as demonstrated in experimental (Ferrari et al., 2015; Ling et al., 2017) and simulation (Tomin and Lunati, 2013, 2015, 2016a,b) studies for unstable viscous fingering in immiscible two-phase displacement. Similar observations was done in the context of density-driven instabilities (Künze et al., 2014; Elenius et al., 2015). In the last study, the perturbation was scaled down with the simulation resolution which helps to obtain a converged convective dissolution rate for unstable flow in gravity currents. Following these ideas, we analyze average characteristics for acidizing process such as wormhole breakthrough time or average porosity profiles.

Governing Equations

In this section, we introduce main governing equations used in the model.

Conservation of Species

Mass conservation equation for i^{th} fluid component is given by

$$\frac{\partial}{\partial t}(\phi \rho_T z_i) + \nabla \cdot \sum_{j=1}^{n_p} (\rho_j x_{ij} \vec{v}_j - \rho_j S_j \phi D_{ij} \nabla x_{ij}) = \sum_k^{n_r} \nu_{ik} r_k, \tag{1}$$

where:

ϕ – porosity,

ρ_T – total density of fluids,

z_i – mole fraction of i^{th} component,

ρ_j – molar density of j^{th} fluid phase,

x_{ij} – molar fraction of fluid component i in phase j,

$\vec{v}_j$ – velocity of fluid phase,

S_j – saturation of fluid phase,

D_{ij} – diffusion coefficient,

ν_{ik} – stoichiometric coefficient for component i in reaction k,

r_k – reaction rate,

n_p – number of phases,

n_r – number of reactions.

The solid species are dissolved into the fluid phase and the solid concentration decay can be accounted as

$$\frac{\partial C_s}{\partial t} = \sum_k^{n_r} \nu_{sk} r_k, \tag{2}$$

where C_s is the solid concentration over the control volume (Fan et al., 2010, 2012; Farshidi et al., 2013). Notice that the fluid molar fractions are defined over the net fluid (i.e. pore) volume and the solid concentration is defined over the entire control volume which includes fluids and solids.

Momentum Conservation

As it was described in the introduction, we assume that the flow is purely single phase in the region with strong porosity changes. Then for fluid velocity, v_j, we have

$$-\nabla p + \frac{\mu_j}{\phi} \Delta \vec{v}_j - \frac{\mu_j}{K} \vec{v}_j = 0, \tag{3}$$

i.e. Darcy-Brinkman-Stokes momentum balance equation (see, e.g. Soulaine and Tchelepi, 2016). Here $\Delta \vec{v}_j$ is the Laplacian of velocity, μ_j the viscosity, K the absolute permeability. The second term in the equation describes fluid-fluid viscous forces, where viscosity is an effective viscosity given by $\mu' = \mu/\phi$. Although there is no clear consensus on the application of effective viscosity (Nield and Bejan, 2006),

numerical simulations by Ochoa-Tapia and Whitaker (1998) confirm that the effective viscosity is indeed increased by a multiplier of $1/\phi$ (see also Goyeau et al., 2003; Bousquet-Melou et al., 2002; Hsu and Cheng, 1990; Vafai and Tien, 1981; Soulaine and Tchelepi, 2016; Soulaine et al., 2016, 2017, for details).

In the multiphase region, we employ classical Darcy's law

$$\vec{v}_j = -\frac{Kk_{rj}(S_j)}{\mu_j}\nabla p = -K\lambda_j \nabla p_j, \tag{4}$$

where k_{rj} is the relative phase permeability (function of phase saturation) and λ_j is the phase mobility. Due to the higher mobility of gas, we assume that the multiphase flow only occurs at low porosity and can be neglected in the regions with high porosity. For simplicity, buoyancy effects are neglected here.

Closure Constraints

Several additional constraints including the assumption on instantaneous thermodynamic equilibrium for multiphase systems are applied to provide the closure of mathematical formulation.

- Instantaneous thermodynamical equilibrium for all components in all existing phases

$$f_{i1} - f_{ij} = 0,\ j = 2,\ldots,n_p,\ i = 1,\ldots,n_c, \tag{5}$$

  where f_{ij} is the fugacity of component i in phase j (function of pressure and composition), n_c is the number of components. Equation (5) is highly nonlinear and should be solved simultaneously with the system of governing equations (1).

- Composition and saturation constraints

$$\sum_i x_{ij} = 1,\ j = 1,\ldots,n_p, \tag{6}$$

$$\sum_j S_j = 1. \tag{7}$$

Chemical Reactions

For simplicity, we limit consideration to a single chemical reaction, which is assumed to be a simple first-order kinetic reaction consistent with dissolution of rock by acid:

$$\text{Acid} + \text{Solid} \rightarrow \text{Product},$$

where the reaction rate is given by

$$r = \alpha C_s z_{acid}. \tag{8}$$

Here α is the reaction rate constant and z_{acid} is the acid concentration.

Constitutive Relations for Porosity and Permeability

The distinctive feature of reactive transport is that the porosity and permeability fields must be updated as the acid dissolves the solid matrix. This porosity increase has a direct relationship with the remaining amount of solid concentration left, which is given by

$$\phi_{ref} = \phi_{ref}^{init} + (v_s^{init} - v_s), \tag{9}$$

where $v_s = C_s v_s^m$ is the volumetric fraction of solid concentration in the control volume and $v_s^{init} = C_s^{init} v_s^m$ is the initial volumetric fraction of the solid (v_s^m is the molar volume). The difference between v_s and

v_s^{init} address the amount of solid volumetric fraction dissolved, i.e. the amount of porosity increase in the control volume.

The updated values of ϕ_{ref} are used to compute the porosity field due to the pressure change

$$\phi = \phi_{ref}\left[1 - c_r(p - p_{ref})\right], \tag{10}$$

where c_r is the rock compressibility, p the pressure, p_{ref} the reference pressure.

Since porosity and permeability are strongly related, the permeability field should be corrected after the dissolution of solid rock. In this study, we employ a Kozeny-Carman relationship (Kozeny, 1927; Carman, 1937):

$$K = K^{init}\left(\phi_{ref}/\phi_{ref}^{init}\right)^3\left[(1-\phi_{ref}^{init})/(1-\phi_{ref})\right]^2, \tag{11}$$

where K and K^{init} are the current and initial permeabilities, respectively.

Dimensionless Numbers

The considered physical phenomenon can be characterized by the two dimensionless numbers – Peclet (Pe) and Damkohler (Da) numbers. These numbers can be used to compare different wormhole models and to determine optimal operation regime.

The Damkohler number is defined as the ratio of reaction rate to advection rate and is given by

$$Da = \frac{l\alpha}{V_o},$$

where l and V_o is the characteristic length scale and velocity, respectively. The Peclet number characterizes the ratio of mass transport due to convection and due to diffusion, i.e.

$$Pe = \frac{lV_o}{D}.$$

Numerical Methods

The proposed model is implemented in Automatic Differentiation General Purpose Research Simulator (AD-GPRS) (Voskov et al., 2017; Rin, 2017; Garipov et al., 2018). The coupled system of equations is spatially discretized employing a finite-volume scheme with a two-point flux approximation and a first-order upwind scheme for advection terms. In case of DBS model, there is a separate momentum equation that has to be included in the system, and the velocities at gridblock interfaces are used as independent unknowns (the details are given in Appendix A).

We use a fully implicit scheme and employ the Newton's method to handle the non-linearities. As it is know, coupling with reactions can make the system very stiff and highly nonlinear which ultimately leads to convergence issues (see, e.g. Shaik, 2017). We will address that in the following section where we describe a general approach for dealing with reactions nonlinearities.

Local Nonlinear Solver for Reactions

In case when the reaction rate is given by Eq. 8, the solid concentration equation, Eq. 2, in a semi-discretized form is linear with respect to C_s:

$$C_s - \check{C}_s = \Delta t\, \nu_s \alpha C_s z_{acid}, \tag{12}$$

so that $C_s = \check{C}_s/(1-\Delta t\,\nu_s\alpha z_{acid})$. It is easy to see that there is a critical time step $\Delta t_{cr} = 1/\nu_s\alpha z_{acid}$ so that if Δt is smaller but very close to Δt_{cr}, solution becomes badly conditioned and $C_s \to +\infty$. The situation is

even worse if $\Delta t \gtrsim \Delta t_{cr}$ because it leads to a large negative C_s. Since α can be quite large, the described time step limitation becomes very important. The negative effects of this overshoot on nonlinear convergence were clearly observed by Shaik et al. (2018), and the problem becomes more pronounced for more complicated physics like DBS model. Similar behavior is observed for pressure in so-called negative compressibility problem (Coats, 1980; Wong et al., 2018), related mostly to geothermal applications.

For more general case, the equation for solid species can be eliminated from the full system using a Schur-complement for Jacobian matrix (Farshidi, 2016). Fig. 1 shows a typical matrix structure for a 10 cells 1D problem with multiple fluid components and a single fluid specie. Since equations for solids are local, J_{ss}^{-1} is easy to construct, and the system can be reduced to a pure fluid system $\hat{J}_{ff} = J_{ff} - J_{fs}J_{ss}^{-1}J_{sf}$, which is easier to solve since this system has convenient structure for compositional simulation (Cao, 2002; Voskov and Tchelepi, 2012).

We propose an alternative general technique in which solid unknowns are eliminated on nonlinear level. Indeed, Eq. 2 is essentially a local nonlinear constraint, $F(p, z_i, C_s)$, which can be solved locally for C_s on a cell-by-cell manner (we employ a Newton-type solver). Then $C_s = g(p, z_i)$ and to get the derivatives with respect to solid changes, we apply the inverse theorem approach (Voskov and Tchelepi, 2012; Garipov et al., 2018):

$$\frac{\partial C_s}{\partial p} = \left(\frac{\partial F}{\partial C_s}\right)^{-1} \frac{\partial F}{\partial p}, \tag{13}$$

$$\frac{\partial C_s}{\partial z_i} = \left(\frac{\partial F}{\partial C_s}\right)^{-1} \frac{\partial F}{\partial z_i}. \tag{14}$$

This technique reminds a classic molar formulation proposed in (Collins et al., 1992) for compositional simulation.

The procedure is greatly simplified by the Automatically Differentiable Expression Templates Library (ADETL) (Younis, 2011). If only one nonlinear iteration is employed for local solver, the approach is almost equivalent to the Schur-compliment procedure described above. Since the linear system is reduces and contains only standard fluid unknowns, we can apply an efficient linear solver. In this study we use SAMG library developed by Fraunhofer SCAI (SAMG, 2017; Gries, 2015; Stüben et al., 2017). We found that the local nonlinear solver greatly helps to stabilize the nonlinear convergence (see Fig. 2 for example).

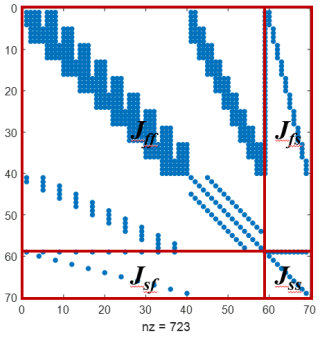

Figure 1 *Typical Jacobian structure for the considered model with 'f' corresponds to fluid and 's' corresponds to solid phases.*

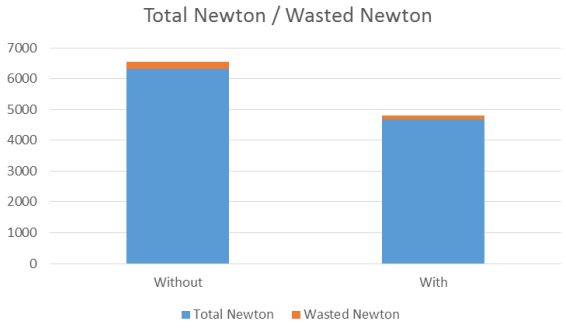

Figure 2 *Comparison of nonlinear solver performance with conventional treatment of reaction (left bar) and with the local reduction (right bar).*

Simulation of Parallel Flow

We start or numerical investigation with a parallel flow model reproducing the numerical setup of Cohen et al. (2008). The study of Cohen et al. (2008) is based on a core-scale non-equilibrium model proposed

Table 1 *Simulation parameters from (Cohen et al., 2008).*

	Property	**Value**
L_y	Height	0.4 m
L_x	Length	0.25 m
ϕ	Initial porosity	0.36
K	Permeability	1.0 mD
ΔK	Permeability perturbation	5 %
α	Reaction rate constant	10 s^{-1}
z_{acid}^{init}	Initial acid concentration	0.0
$z_{H_2O}^{init}$	Initial water concentration	1.0
z_{acid}^{inj}	Concentration of acid in injection	0.75
$z_{H_2O}^{inj}$	Concentration of water in injection	0.25
p_{out}	Pressure boundary condition downstream	100 bar
D	Diffusivity	10^{-9} m^2/s

in (Golfier et al., 2002). An acid is injected into a $25 \times 40 \times 0.1$ cm carbonated sandstone block from the left face at a constant injection rate while the pressure at the downstream boundary is fixed. To mimic a small-scale heterogeneity that in real applications perturbs the flow and leads to the formation of instabilities, a small perturbation is introduced for permeability. The simulation parameters are summarized in Table. 1. More detailed explanation can be found in (Shaik, 2017; Shaik et al., 2018). The variation in the type of wormhole formation with increasing velocity was obtained in Cohen's study. The shape of the wormholes for a given velocity range is consistent with the experimental findings (Golfier et al., 2002) and the later simulation studies (Maheshwari et al., 2013). Notice that a Darcy-type model was used in (Cohen et al., 2008).

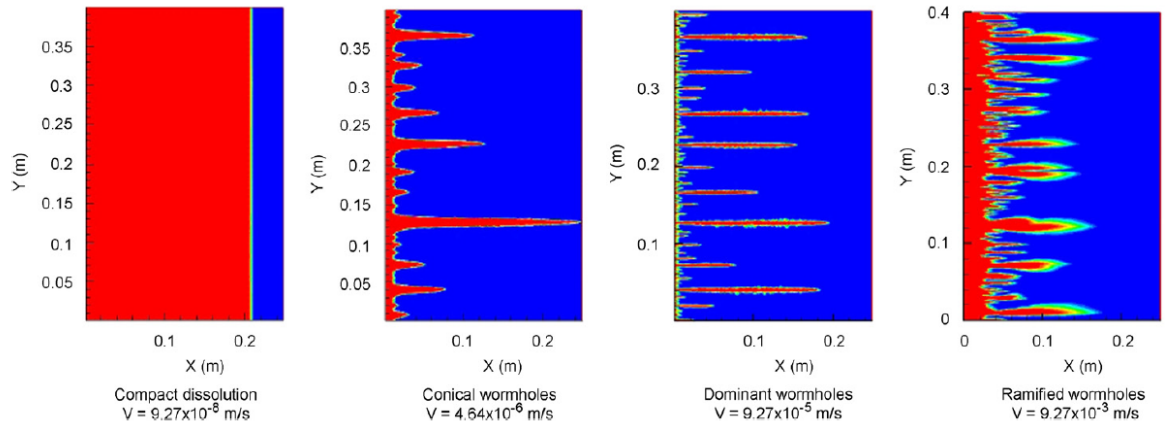

Figure 3 *Cohen et al. (2008) simulation results. Wormhole dissolution patterns for increasing injection velocity. The red field represents fully-dissolved region with 100% porosity. The resolution is 200×800 cells. Reprinted from (Cohen et al., 2008).*

The results, obtained with the proposed framework using the Darcy model after 0.7 pore-volume injected (PVI) are shown in Fig. 4. These results was obtained for the same velocities as in the study of Cohen et al. (2008) and only perturbation pattern and pore-volume injected is different from Fig. 3. Note that even though governing model in (Cohen et al., 2008) is different from our model (mostly due to the treatment of porosity), the framework, proposed in this study, can qualitatively reproduce similar results at specified velocity values. The numerical convergence of results was obtained earlier (at 100×400 cells vs. 200×800 cells) than in (Cohen et al., 2008) as indicated by Shaik et al. (2018).

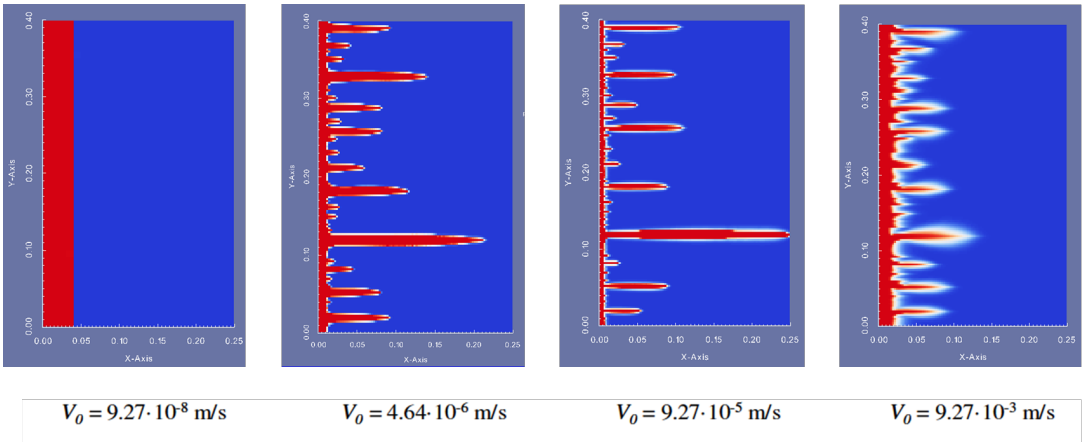

Figure 4 *Wormhole dissolution patterns for increasing injection velocity in the proposed model using Darcy's assumptions with 100×400 cells resolution.*

Effect of Heterogeneity

Keeping the same parameters, we increase the heterogeneity amplitude of permeability for a dominant regime. We used permeability perturbations ΔK of 5%, 10%, and 20%. The porosity distributions for all three amplitudes are shown in Fig. 5. Based on these results, there is a limited sensitivity of the wormhole distribution to the heterogeneity amplitude.

However, this conclusion is changing if we look into the sensitivity of dominant wormhole length as function of time (Fig. 6). It is clear that for $\Delta K = 20\%$ the length of the leading wormhole lags behind for cases with lower amplitude. As the heterogeneity amplitude increases, the number of wormholes increases which leads to less competition between the wormholes. As a result, the breakthrough time grows with the heterogeneity amplitude.

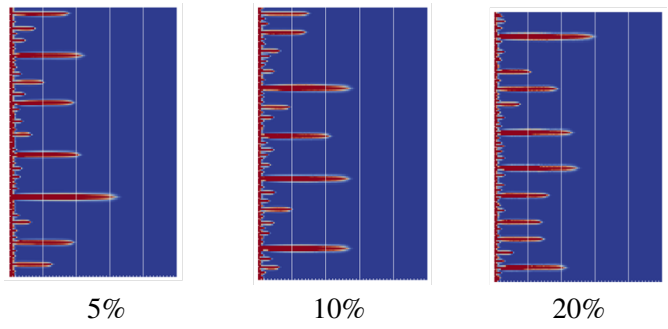

Figure 5 *Porosity maps for Darcy model with different permeability perturbation at dominant regime*

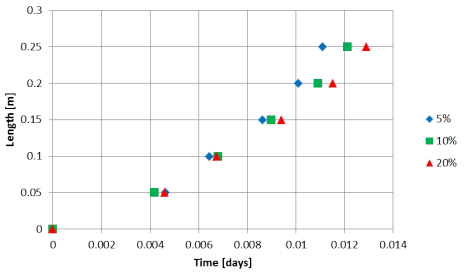

Figure 6 *Wormhole dynamics for permeability perturbation at 5, 10, and 20%.*

Comparison between Darcy and Darcy-Brinkman-Stokes Models

Next, we analyze the difference between Darcy and DBS models at various velocity regimes. The analysis is performed in terms of pore-volume injected until the breakthrough PV_{BT}. We start at low velocity regime where no wormholes observed at the front, which is the compact dissolution regime (see the first image in Fig. 4 for Darcy and Fig. 7 for DBS models respectively). It can be observed as well that the dissolution in the Darcy flow is slightly faster than in the DBS model.

Next, we enter the conical wormhole regime by increasing the injection velocity. In the conical regime, there is a single prominent or leading wormhole that channels most of the incoming flux. That explains much lower PV_{BT} than in the compact regime for both models (see Fig. 8). Here, a more advanced

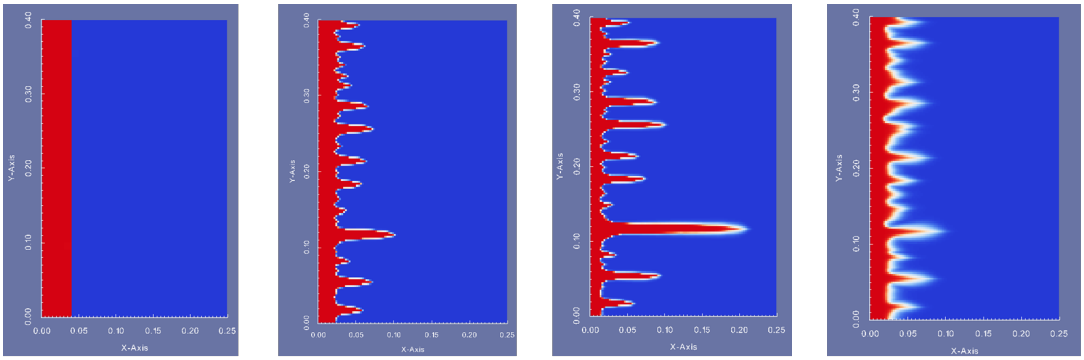

Figure 7 *Wormhole dissolution patterns for increasing injection velocity in the proposed model using DBS description with 100×400 cells resolution.*

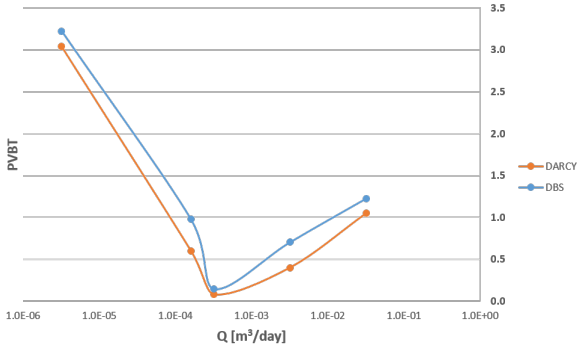

Figure 8 *PV_{BT} analysis for Darcy and DBS models for the resolution of 100×160 cells.*

wormholes belongs to the Darcy regime when DBS-based wormholes are left behind.

With the increasing velocity, the wormholes start thinning due to more dominant dissolution in the tip of wormholes. This is the most effective regime for both Darcy and DBS models as can be seen in Fig. 8. On further increasing the velocity, we can observe more wormholes, carrying the influx and dissolving more rock along it. Once in the dominant regime, there are multiple wormholes without a clear leading wormhole. This slows the breakthrough as illustrated in the Fig. 8. Moving into the ramified regime, there are multiple wormholes but the wormhole tips are now smeared and the penetration into the core is much weaker and hence the PV_{BT} increases. The porosity fields corresponding to the points used in Fig. 8 are shown in Fig. 4.

To conclude, it is clear that the simulation results based on Darcy velocity over-predict the propagation of wormholes. The development of fingers and breakthrough moment happened much later with DBS approach. Using PV_{BT} to quantify the difference in Fig. 8 shows that Darcy model always needs fewer pore volumes for breakthrough than the DBS model. This could be understood by the fact that in the Darcy model, we ignore the dissipative viscous forces term i.e $-\mu'\Delta\vec{V}$. The DBS model takes these losses into account which plays an important role for control volumes with significantly dissolved rock.

Acidization with Gas Co-injection

Unlike the well stimulation projects for oil recovery, the wormhole patterns in CO_2 co-injection are more complicated due to the presence of the second phase. The single-phase acidization is governed and optimized with dimensionless numbers such as Peclet and Damkohler numbers by changing the flow rate, acid type, permeability field as discussed in the previous sections. While the single-phase acidizing with an acid (liquid phase) injection occurs through matrix dissolution, it becomes quite different with

CO_2 co-injection. The CO_2 first dissolves in the fluid phase and forms carbonic acid (H_2CO_3) which in turn dissolves the matrix. This delayed dissolution leads to a deeper penetration and hence a better acid job as a consequence. Therefore, a co-injection of CO_2 and acid such as HCl could yield a better and quicker breakthrough result in case carbonic acid can be formed.

In the present study, we simulate the effect of CO_2 co-injection along with an immiscible acid component. The net volumetric injection rate of the acid is kept the same as previous experiments while the net CO_2 mole fraction is 0.1 now. In our simulations, we ignored the formation of carbonic acid. That is why not much of a difference is observed in the pore volume needed for breakthrough in both Darcy and DBS models, which is evident from Figs. 9 and 10.

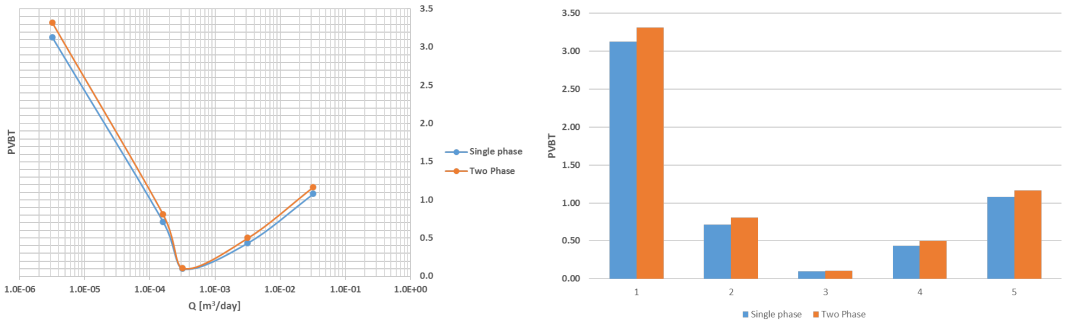

Figure 9 *PVBT analysis of two-phase injection and comparison with single-phase case (Darcy model).*

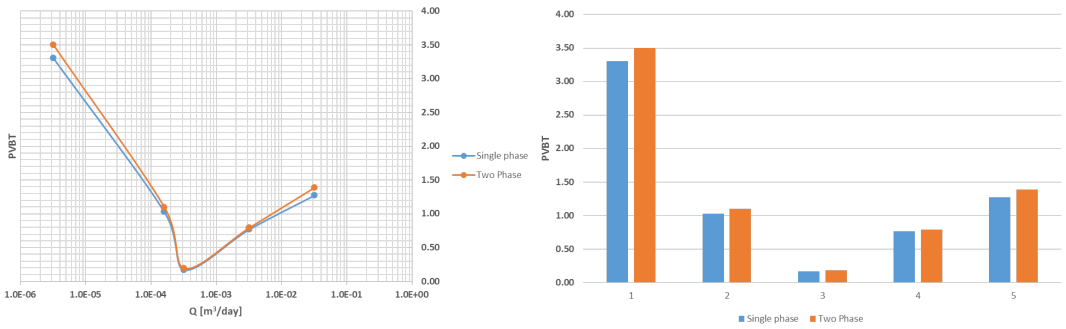

Figure 10 *PVBT analysis of two-phase injection and comparison with single-phase case (DBS model).*

The PVBT plots obtained for two-phase co-injection reveal a slight increase in pore volumes needed for breakthrough, consistent with the experimental studies by Ott and Oedai (2015). A closer look must be taken at the CO_2 concentration and its localization in order to understand the reason for the delayed breakthrough. Also, the DBS model, used here, does not include an accurate treatment of two phase flow in momentum equations and can only be seen as an idealistic approximation.

The physical phenomenon for the inhibition of the wormholes can be understood by observing Fig. 11. As the wormholes are formed by the reactive liquid phase, the CO_2 in the gas phase rushes into the dissolved wormhole channels. Also, since CO_2 has a higher mobility than the liquid phase, it propagates into the porous media around the wormholes. Since CO_2 is not reactive in this case, it prevents the reactive acid from penetration further into the porous matrix, thereby leading to a net inhibition and accounting to a higher PVBT than in the single-phase case. This is consistent with the experimental and simulation studies performed by Izgec et al. (2008) in which the retardation of the wormhole growth was recorded in a CT scan.

Simulation of Radial Flow

Here, we perform a radial flow simulation and quantify the difference between Darcy and DBS models. We consider a 3D cylindrical domain of radius $R_d = 10.0$ m with a well in the center, well radius is

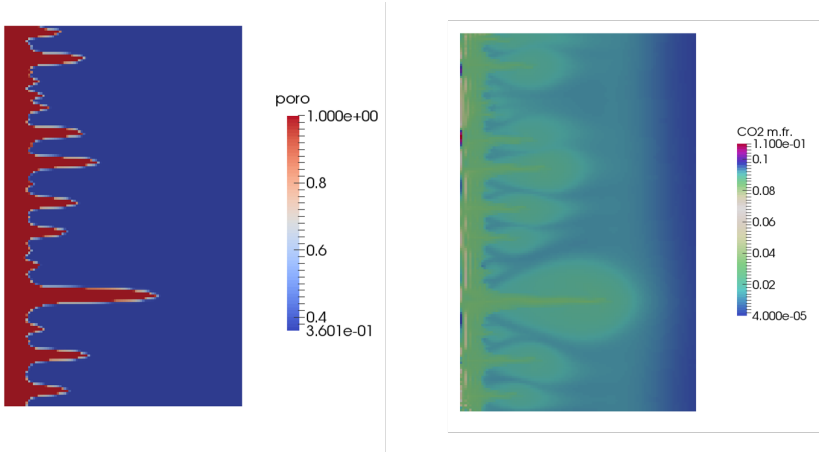

Figure 11 *Smearing and retardation of wormholes due to CO_2 co-injection. Left: porosity field of conical wormhole. Right: CO_2 concentration around wormhole.*

$r_w = 0.1$ m. The pressure is fixed at the outer boundary, and a fixed injection rate is prescribed for the well. The initial porosity is 0.3. The rest of the model parameters are the same as in the previous example. To discretize the domain, we use a triangular prism mesh generated using Gmsh (Geuzaine and Remacle, 2009) which makes the model discretization 2.5D. The triangular mesh gives an additional perturbation that helps to trigger and capture instabilities. An example of a low-resolution mesh with 19 114 cells is shown in Fig. 12.

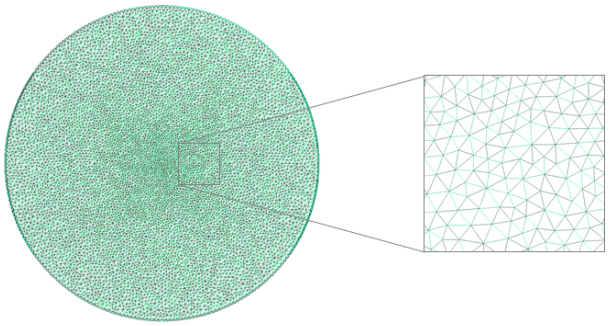

Figure 12 *An example of triangular prism mesh used in simulations. The mesh has 19 114 cells.*

Effects of Heterogeneity and Grid Resolution

We start with a small perturbation of 1% and gradually increase it up to 5% and 25%. Significant local differences can be observed (Fig. 13, left), however for average quantities such as the breakthrough time and average porosity profile in radial direction, the sensitivity to the heterogeneity amplitude is very limited, similar to the previous example. The porosity profiles for the three cases (Fig. 13, right) are very close to each other. However, as can be seen from the dissolution contours in Fig. 13 (left), the breakthrough takes slightly longer time for larger perturbation. That confirms our previous observations. In the following simulations, we use the perturbation of 5%.

We also observe that in radial geometry, instabilities in the wormhole propagation are more sensitive to the perturbation scale (cell size). It is much more complicated to consistently upscale the perturbation in unstructured geometry comparing to the Cartesian grids (Elenius et al., 2015). In Fig. 14, we show the comparison between three different resolutions. The grids were generated by changing the maximum cell size, $\Delta h_{\max}$. As you can see, the structure of unstable wormholes is strongly dependent on the resolution and scale of perturbation. However, when breakthrough characteristics are compared (see Fig. 15), no large differences are observed between the resolutions.

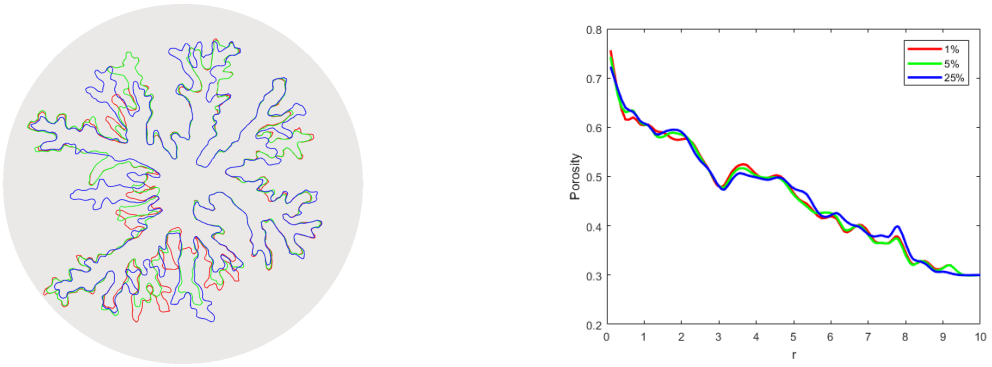

Figure 13 *Dissolution contour (left) and average porosity profile (left) for different permeability perturbation levels. Colors: red – 1%, green – 5%, blue – 25% perturbation.*

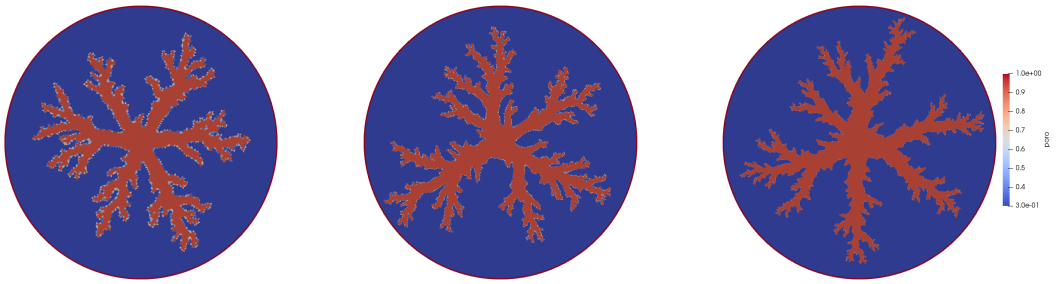

$\Delta h_{\max} = 0.2$	$\Delta h_{\max} = 0.1$	$\Delta h_{\max} = 0.05$
21 425 cells	82 518 cells	336 334 cells

Figure 14 *Porosity maps for different grid resolutions.*

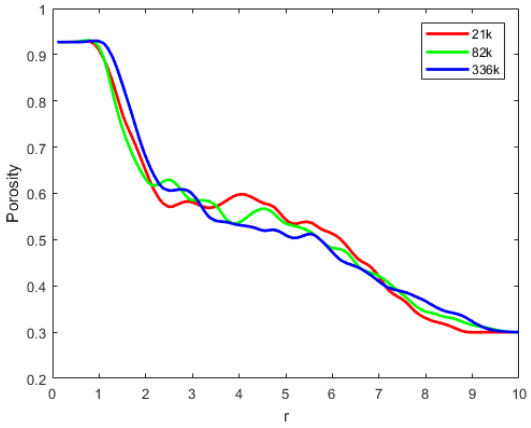

Figure 15 *Average porosity profiles for different grid resolutions.*

Comparison between Darcy and Darcy-Brinkman-Stokes Models

Next, similar to the previous study, we compare Darcy and DBS simulations. Based on multiple numerical experiments, we conclude that the numerical behavior of Darcy vs. DBS models in radial geometry is similar to the parallel flow. In Fig. 16, you can see a typical comparison between results produced by these two models. While the wormholes in Darcy model propagate farther and demonstrate strong fractal structure, in the DBS model, the wormholes propagate slower and their structure is smooth.

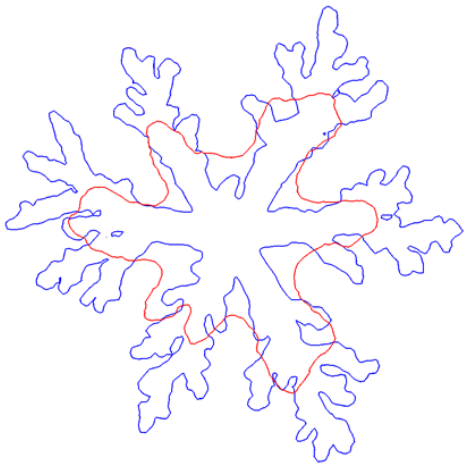

Figure 16 *Dissolution contour for Darcy model (blue) and DBS model (red).*

Conclusions

We presented a fully coupled formulation and simulation framework for modeling of acid stimulation at continuum scale. The Darcy-Brinkman-Stokes (DBS) approach is adopted to accurately represent regions with high porosity. The system of equations for multiphase multicomponent reactive flow and transport is solved fully implicitly together with a momentum balance DBS equation for fluid and a mass balance equation for solid species. For solids dissolution, we developed a local nonlinear solver that acts in a cell-by-cell manner and allows dealing with the balance of solids separately yet retaining the full coupling with rest of the equations. The solver helps to stabilize the convergence and to reduce the size of the linear system. We compared the dissolution patterns for classical Darcy and extended DBS models and studied the impact of multiphase flow. For the DBS approach, we employed a hybrid technique, where we assume that the single-phase DBS flow and the multiphase Darcy flow occur in separate regions. The simulation results were reported for both structured linear and unstructured radial geometries.

Acknowledgements

We thank Kirill Terekhov and Cyprien Soulaine for useful discussion, and Rahman Shaik for his contribution at the early stage of this work.

References

AD-GPRS [2018] Automatic Differentiation General Purpose Research Simulator (AD-GPRS). Stanford University, `https://supri-b.stanford.edu/research-areas/ad-gprs`.

Bousquet-Melou, P., Goyeau, B., Quintard, M., Fichot, F. and Gobin, D. [2002] Average momentum equation for interdendritic flow in a solidifying columnar mushy z one. *International journal of heat and mass transfer*, **45**(17), 3651–3665.

Brinkman, H. [1949] A calculation of the viscous force exerted by a flowing fluid on a dense swarm of particles. *Applied Scientific Research*, **1**(1), 27–34.

Cao, H. [2002] *Development of Techniques for General Purpose Simulators*. PhD Thesis, Stanford University.

Carman, P.C. [1937] Fluid flow through granular beds. *Transactions-Institution of Chemical Engineeres*, **15**, 150–166.

Coats, K.H. [1980] Reservoir Simulation: a General Model Formulation and Associated Physical/Numerical Sources of Instability. *Boundary and Interior Layers - Computational and Asymptotic Methods*, 62–76.

Cohen, C.E., Ding, D., Quintard, M. and Bazin, B. [2008] From pore scale to wellbore scale: Impact of geometry on wormhole growth in carbonate acidization. *Chemical Engineering Science*, **63**(12),

3088–3099.

Collins, D., Nghiem, L., Li, Y.K. and Grabonstotter, J. [1992] An Efficient Approach to Adaptive-Implicit Compositional Simulation With an Equation of State. *SPE*, **15133-PA**.

Earlougher Jr, R.C. [1977] Advances in Well Test Analysis, Henry L. *Doherty series, Monograph*, **5**.

Elenius, M., Voskov, D. and Tchelepi, H. [2015] Interactions between gravity currents and convective dissolution. *Advances in Water Resources*, **83**, 77–88.

Fan, Y., Durlofsky, L. and Tchelepi, H.A. [2010] Numerical simulation of the in-situ upgrading of oil shale. *SPE Journal*, **15**(02), 368–381.

Fan, Y., Durlofsky, L.J. and Tchelepi, H.A. [2012] A fully-coupled flow-reactive-transport formulation based on element conservation, with application to CO 2 storage simulations. *Advances in Water Resources*, **42**, 47–61.

Farshidi, S.F. [2016] *Compositional Reservoir Simulation-based Reactive-transport Formulations, with Application to CO2 Storage in Sandstone and Ultramafic Formations*. Ph.D. thesis, Stanford University.

Farshidi, S.F., Fan, Y., Durlofsky, L.J. and Tchelepi, H.A. [2013] Chemical Reaction Modeling in a Compositional Reservoir-Simulation Framework. In: *SPE Reservoir Simulation Symposium*. Society of Petroleum Engineers.

Ferrari, A., Jimenez-Martinez, J., Borgne, T.L., Méheust, Y. and Lunati, I. [2015] Challenges in modeling unstable two-phase flow experiments in porous micromodels. *Water Resources Research*, **51**(3), 1381–1400.

Garipov, T., Tomin, P., Rin, R., Voskov, D. and Tchelepi, H. [2018] Unified Thermo-Compositional-Mechanical Framework for Reservoir Simulation. *Computational Geosciences*.

Geuzaine, C. and Remacle, J.F. [2009] Gmsh: A 3-D finite element mesh generator with built-in pre- and post-processing facilities. *International journal for numerical methods in engineering*, **79**(11), 1309–1331.

Golfier, F., ZArcone, C., Bazin, B., Lenormand, R., Lasseux, D. and Quintard, M. [2002] On the ability of a Darcy-scale model to capture wormhole formation during the dissolution of a porous medium. *Journal of fluid Mechanics*, **457**, 213–254.

Goyeau, B., Lhuillier, D., Gobin, D. and Velarde, M. [2003] Momentum transport at a fluid–porous interface. *International Journal of Heat and Mass Transfer*, **46**(21), 4071–4081.

Gries, S. [2015] *System-AMG Approaches for Industrial Fully and Adaptive Implicit Oil Reservoir Simulations*. Ph.D. thesis, Universität zu Köln.

Hsu, C. and Cheng, P. [1990] Thermal dispersion in a porous medium. *International Journal of Heat and Mass Transfer*, **33**(8), 1587–1597.

Izgec, O., Demiral, B., Bertin, H. and Akin, S. [2008] CO2 injection into saline carbonate aquifer formations. *Transport in Porous Media*, **72**(1), 1–24.

Kalfayan, L. [2008] *Production enhancement with acid stimulation*. Pennwell Books.

Kozeny, J. [1927] Uber kapillare leitung der wasser in boden. *Royal Academy of Science, Vienna, Proc. Class I*, **136**, 271–306.

Künze, R., Tomin, P. and Lunati, I. [2014] Local modeling of instability onset for global finger evolution. *Advances in water resources*, **70**, 148–159.

Ling, B., Bao, J., Oostrom, M., Battiato, I. and Tartakovsky, A.M. [2017] Modeling variability in porescale multiphase flow experiments. *Advances in Water Resources*, **105**, 29–38.

Maheshwari, P., Ratnakar, R., Kalia, N. and Balakotaiah, V. [2013] 3-D simulation and analysis of reactive dissolution and wormhole formation in carbonate rocks. *Chemical Engineering Science*, **90**, 258–274.

Nield, D.A. and Bejan, A. [2006] *Convection in porous media*, 3. Springer.

Ochoa-Tapia, J.A. and Whitaker, S. [1998] Heat transfer at the boundary between a porous medium and a homogeneous fluid: the one-equation model. *Journal of Porous Media*, **1**(1).

Olshanskii, M.A., Terekhov, K.M. and Vassilevski, Y.V. [2013] An octree-based solver for the incompressible Navier–Stokes equations with enhanced stability and low dissipation. *Computers & Fluids*, **84**, 231–246.

Ott, H. and Oedai, S. [2015] Wormhole formation and compact dissolution in single-and two-phase CO2-brine injections. *Geophysical Research Letters*, **42**(7), 2270–2276.

Perot, B. [2000] Conservation properties of unstructured staggered mesh schemes. *Journal of Compu-*

tational Physics, **159**(1), 58–89.
Perot, B. and Nallapati, R. [2003] A moving unstructured staggered mesh method for the simulation of incompressible free-surface flows. *Journal of Computational Physics*, **184**(1), 192–214.
Rin, R. [2017] *Implicit Coupling Framework for Multi-Physics Reservoir Simulation*. Ph.D. thesis, Stanford University.
Rin, R., Tomin, P., Garipov, T., Voskov, D. and Tchelepi, H. [2017] General Implicit Coupling Framework for Multi-Physics Problems. In: *SPE Reservoir Simulation Conference*. Society of Petroleum Engineers.
SAMG [2017] Algebraic Multigrid Processes for Systems (SAMG). Fraunhofer SCAI, `http://scai.fraunhofer.de/samg`.
Shaik, A., Tomin, P. and Voskov, D. [2018] Modeling of Near-Well Matrix Acidization. In: *43rd Workshop on Geothermal Reservoir Engineering*.
Shaik, R. [2017] *Modelling of Near-Well Acidisation*. Master's thesis, TU Delft.
Soulaine, C., Gjetvaj, F., Garing, C., Roman, S., Russian, A., Gouze, P. and Tchelepi, H.A. [2016] The impact of sub-resolution porosity of X-ray microtomography images on the permeability. *Transport in Porous Media*, **113**(1), 227–243.
Soulaine, C., Roman, S., Kovscek, A. and Tchelepi, H.A. [2017] Mineral dissolution and wormholing from a pore-scale perspective. *Journal of Fluid Mechanics*, **827**, 457–483.
Soulaine, C. and Tchelepi, H.A. [2016] Micro-continuum approach for pore-scale simulation of subsurface processes. *Transport in Porous Media*, **113**(3), 431–456.
Stüben, K., Ruge, J.W., Clees, T. and Gries, S. [2017] Algebraic Multigrid: From Academia to Industry. In: *Scientific Computing and Algorithms in Industrial Simulations*, Springer, 83–119.
Tomin, P. and Lunati, I. [2013] Hybrid Multiscale Finite Volume method for two-phase flow in porous media. *Journal of Computational Physics*, **250**, 293–307.
Tomin, P. and Lunati, I. [2015] Local–global splitting for spatiotemporal-adaptive multiscale methods. *Journal of Computational Physics*, **280**, 214–231.
Tomin, P. and Lunati, I. [2016a] Investigating Darcy-scale assumptions by means of a multiphysics algorithm. *Advances in water resources*, **95**, 80–91.
Tomin, P. and Lunati, I. [2016b] Spatiotemporal adaptive multiphysics simulations of drainage-imbibition cycles. *Computational Geosciences*, **20**(3), 541–554.
Vafai, K. and Tien, C. [1981] Boundary and inertia effects on flow and heat transfer in porous media. *International Journal of Heat and Mass Transfer*, **24**(2), 195–203.
Voskov, D.V., Henley, H. and Lucia, A. [2017] Fully compositional multi-scale reservoir simulation of various CO2 sequestration mechanisms. *Computers and Chemical Engineering*, **96**, 183 – 195.
Voskov, D.V. and Tchelepi, H.A. [2012] Comparison of nonlinear formulations for two-phase multi-component EoS based simulation. *Journal of Petroleum Science and Engineering*, **82-83**, 101 – 111.
Wong, Z.Y., Horne, R.N. and Tchelepi, H.A. [2018] Sequential implicit nonlinear solver for geothermal simulation. *Journal of Computational Physics*, **368**, 236–253.
Younis, R.M. [2011] *Modern advances in software and solution algorithms for reservoir simulation*. Ph.D. thesis, Stanford University.

Appendix

Discretization of Momentum Equation

Here we briefly describe how we discretize the momentum balance, Eq. 3, see, e.g. (Olshanskii et al., 2013; Perot, 2000; Perot and Nallapati, 2003) for details. For simplicity of the description we assume scalar absolute permeability and constant viscosity.

We start from introducing the velocity unknowns: $q_f = \vec{V}\vec{n}_f A_f$, which are phase fluxes through cell faces. Here $\vec{n}_f$ is the face normal and A_f is the face surface.

For single-phase Darcy's law we usually have the following projection on the face (TPFA scheme):

$$q_f = -\frac{1}{\mu}\left(K\nabla p\right)_f \vec{n}_f A_f = -\frac{1}{\mu} T_f \left(\Delta p\right)_f, \tag{15}$$

where $T_f = K_f A_f$ is the transmissibility ($K_f = 2/(d_1/K_1 + d_2/K_2)$), $(\Delta p)_f = p_1 - p_2$ is the pressure difference.

Full projection of Eq. 3 has the form

$$-\frac{1}{\mu} T_f (\Delta p)_f + \frac{1}{\phi_f} (K \Delta \vec{V})_f \vec{n}_f A_f - q_f = 0, \tag{16}$$

where $(\phi)_f = (\phi_1 + \phi_2)/2$ is the porosity on the face. In Eq. 16, the main issue is to approximate the Brinkman term, which is done with the following algorithm:

1. Cell-centered velocity can be reconstructed from q_f as following

$$\vec{V}_c = \frac{1}{v_\Omega} \sum_{f \in \partial\Omega} q_f (\vec{x}_f - \vec{x}_c), \tag{17}$$

   where v_Ω is the cell volume, $\vec{x}_c$ is the position of the cell center, $\vec{x}_f$ are the positions of centers of the cell faces.

2. Compute the velocity Laplacian in the cell center using the two-point approximation

$$\left(\Delta \vec{V}\right)_c = \nabla \cdot (\nabla \vec{v}) = \frac{1}{v_\Omega} \sum_{f \in \partial\Omega} (\nabla \vec{v})_f \vec{n}_f A_f = \frac{1}{v_\Omega} \sum_{f \in \partial\Omega} T_f^v (\Delta \vec{v}_c)_f, \tag{18}$$

   where $\left(\Delta \vec{V}_c\right)_f = \vec{V}_{cf} - \vec{V}_c$ and $T_f^v = A_f/(d_1 + d_2)$.

3. Finally project the $\left(\Delta \vec{V}\right)_c$ to the face

$$(K \Delta \vec{V})_f \vec{n}_f A_f = \left(\Delta \vec{V}\right)_f \vec{n}_f K_f A_f = \left[\left(\Delta \vec{V}\right)_{c,1} (\vec{x}_f - \vec{x}_1) - \left(\Delta \vec{V}\right)_{c,2} (\vec{x}_f - \vec{x}_2)\right] T_f. \tag{19}$$

If no-slip boundary condition, $\vec{V}|_\Gamma = \vec{0}$, is required, it simply should be accounted in the Laplacian computation (Eq. 18), and for $f \in \Gamma$ we have

$$T_f^v \left(\Delta \vec{V}_c\right)_f = -T_f^v \vec{V}_c, \tag{20}$$

where

$$T_f^v = \frac{A_f}{d}, \tag{21}$$

d is the distance to the face from the cell center.